International Journal of Heat and Mass Transfer 221 (2024) 125063

Contents lists available at ScienceDirect

International Journal of Heat and Mass Transfer

journal homepage: www.elsevier.com/locate/ijhmt

Predictability of thermoelectric figure of merit for the single crystal from first principles

Jinlong Ma [a], Yani Chen [c], Wu Li [b,c,*], Xiaobing Luo [a,*]

[a] School of Energy and Power Engineering, Huazhong University of Science and Technology, Wuhan 430074, China
[b] Eastern Institute for Advanced Study, Eastern Institute of Technology, Ningbo 315200, China
[c] Institute for Advanced Study, Shenzhen University, Shenzhen 518060, China

ARTICLE INFO

Keywords:
Thermoelectric
First-principles
SnSe
Pressure

ABSTRACT

The first-principles calculations have been widely used to predict the thermoelectric figure of merit (ZT) for the single crystal, but such precise calculations are confined to phonon-limited intrinsic system, and the defects present in practical samples cannot be easily modeled. So, a question arises as to whether the phonon-limited ZT can represent the thermoelectric potential of the material. In this work, we demonstrate that the exclusion of defect scattering could provide ZT close to the actual values in single crystal by analyses of the ZT involved parameters. This is also illustrated in the case of SnSe by performing first-principles calculations of phonon-limited ZT compared with available experimental data. The calculated ZT can reproduce the measured values, indicating that the calculations possess predictive capability. On the basis, strong and anisotropic thermoelectric enhancement of SnSe induced by pressure is found. The pressure significantly increases the thermoelectric power factor of *n*-type SnSe along its *a* crystallographic axis and that of *p*-type SnSe along the *b* axis, while the increase of lattice thermal conductivity is relatively small. As a result, a large enhancement of ZT is obtained. By applying pressure up to 3.2 GPa, at room temperature, the *a*-axis ZT of *n*-type SnSe is as high as 1.2, while the *b*-axis ZT of *p*-type SnSe reaches up to 0.8, which are more than twice larger than the values at ambient pressure. This study provides strong confidence and support for the application of first-principles calculations to search high-performance thermoelectric materials and thus would be an important reference for future researches.

1. Introduction

Thermoelectric technology enables direct and reversible conversion between heat and electricity, which provides a promising solution in waste heat recovery and electronic refrigeration. The key to the popularization of practical applications lies in the energy conversion efficiency of thermoelectric materials, which is determined by the dimensionless figure of merit $ZT = \alpha^2\sigma T/(\kappa_e + \kappa_l)$, where α is the Seebeck coefficient, σ is the electrical conductivity, T is the absolute temperature, κ_e and κ_l are the thermal conductivities contributed by electron transport and phonon transport, respectively. Finding materials with high ZT is the essential demand for the enhancement of thermoelectric performance. Theoretical prediction is an efficient way to screen out high ZT candidates from thousands of systems at a small cost as compared to experiments. The primary task is the accurate calculations of ZT involved transport properties. In pristine single crystals, the intrinsic κ_l and $\{\alpha, \sigma, \kappa_e\}$ are limited by the phonon-phonon and electron-phonon interactions, respectively, which can be extracted from density functional theory (DFT) and density functional perturbation theory (DFPT) calculations. Combined with Boltzmann transport equations (BTE), the phonon and electron transport properties can be obtained in the parameter-free framework at first-principles accuracy. The first-principles calculations of intrinsic κ_l have been well developed in the past decades [1–3] and have been widely used to search thermoelectric candidates with low-κ_l following the phonon-glass electron-crystal paradigm [4,5]. The calculations of intrinsic $\{\alpha, \sigma, \kappa_e\}$ have also been achieved in first-principles framework recently and have been successfully applied to many materials with satisfactory results [6–9]. Therefore, it is already feasible to derive the phonon-limited ZT by predicting all relevant quantities through the first-principles calculations [10–13].

In practical applications, the single crystals generally contain intermediate or strong doping, bringing defects into crystal structures. However, modeling the defects with predictive accuracy cannot be eas-

* Corresponding author.
E-mail addresses: wu.li.phys2011@gmail.com (W. Li), luoxb@hust.edu.cn (X. Luo).

https://doi.org/10.1016/j.ijheatmasstransfer.2023.125063
Received 19 October 2023; Received in revised form 22 November 2023; Accepted 8 December 2023
Available online 14 December 2023

ily achieved for two reasons: first it is hard to acquire the knowledge of defects experimentally, and second it lacks powerful treatment of defects in calculations. Recently, the calculations of defects-included phonon transport [14,15] and electron transport [16,17] have been demonstrated with high accuracy by calculating the perturbation matrix of supercells including defects. Nonetheless, only simple types of point defects like substitutions and vacancies can be considered and the computational cost for perturbed supercell system is dramatically multiplied as compared to that of traditional treatment on primitive cell. Furthermore, single crystals are the parent materials for the thermoelectric enhancement. Therefore, the calculation without considering defects is still the priority choice in terms of rapid pre-research. As a matter of course, a concern arises about whether the phonon-limited ZT does represent the thermoelectric potential of materials.

To evidence the ability of first-principles calculations in ZT prediction for single crystals, SnSe is a rather ideal alternative for comparing calculations and experiments due to its numerous measurements of *n*- and *p*-type doped systems. SnSe has anisotropic layered crystal structure and undergoes continuous phase transition from *Pnma* to *Cmcm* phase starting around 600 K to the critical temperature of 800 K [18–20]. The remarkable thermoelectric properties of SnSe were first noticed by Zhao et al. [18], reporting an unprecedented high ZT of 2.6±0.3 at 923 K in the unintentionally doped *p*-type system along the *b* axis direction due to its intrinsically ultralow lattice thermal conductivity. The authors later realized heavy hole doping in single crystals of SnSe successfully by introducing sodium dopants, and the ZT was vastly increased to 0.7 at 300 K while the maximum ZT reaches up to 2.0 at 773 K along the *b* axis direction owing to the enhanced electrical conductivity and Seebeck coefficient afforded by doping [21]. Subsequently, *n*-type SnSe was obtained via bismuth doping, achieving a ZT value of 2.2 at 733 K along the *b* axis direction [22]. The *n*-type SnSe was also synthesized through bromine doping, which generates overlapping interlayer charge density to form three-dimensional charge transport but remains two-dimensional phonon transport in the out-of-plane direction, resulting in a record ZT value of 2.8±0.5 at 773 K [19]. The average ZT at 300 to 773 K was further improved in chlorine-doped, lead-alloyed and copper-doped SnSe by multi-band synglisis, phonon-electron decoupling and lattice plainification [23–25].

Previously, Li et al. [12] have used first-principles methods to calculate the ZT of *Pnma* SnSe, taking into account the effect of point dopant scattering in phonon transport with an empirical simplified formula but not in electron transport. The obtained ZT at 300 K for *n*- and *p*-type SnSe are acceptable as compared with the experiments of Chang et al. [19] and Zhao et al. [21], respectively. In contrast to this research, we focus on the comparison between calculated ZT of defect-free crystals and experimental values at more comprehensive temperatures and carrier concentrations. Another issue to be aware of is that the thermoelectric performance of *Pnma* SnSe can be enhanced by pressure [26,27] due to the changes in crystal structure and thus leading to a certain influence on electron and phonon properties. Recent experiments have demonstrated that the pressure induces Lifshitz transition in *Pnma* SnSe and thus largely enhances the thermoelectric power factor over a large temperature range [28]. However, previous calculations adopted constant [26] and simplified empirical [27] approximations for electron-phonon scattering, which may cause large deviations from the real physical processes especially for such highly anisotropic materials. Therefore, in this work, we calculated all the ZT involved transport properties of *Pnma* SnSe using fully first-principles methods. It is found that the measured ZT does not deviate from the calculated values significantly, demonstrating the speculation that the calculation without including the defect scattering is able to reveal the thermoelectric promise of single crystals. On this basis, the ZT of *Pnma* SnSe under different pressures are investigated. By applying pressure, the ZT of *n*- and *p*-type SnSe are significantly enhanced in the *a*- and *b*-axis directions, respectively, but no obvious improvement in other directions.

2. Methodology

The electrical transport properties of $\boldsymbol{\sigma}$, $\boldsymbol{\alpha}$ and $\boldsymbol{\kappa}_e$ can be derived from the framework of BTE for electron, as [11,29]

$$\boldsymbol{\sigma} = \frac{se^2}{\Omega N_{\mathbf{k}}} \sum_{n\mathbf{k}} \mathbf{v}_{n\mathbf{k}} \mathbf{F}_{n\mathbf{k}} \left(-\frac{\partial f^0_{n\mathbf{k}}}{\partial \varepsilon_{n\mathbf{k}}}\right), \tag{1}$$

$$\boldsymbol{\alpha} = \frac{\boldsymbol{\sigma}^{-1} se}{T\Omega N_{\mathbf{k}}} \sum_{n\mathbf{k}} (\varepsilon_{n\mathbf{k}} - \varepsilon_f) \mathbf{v}_{n\mathbf{k}} \mathbf{F}_{n\mathbf{k}} \left(-\frac{\partial f^0_{n\mathbf{k}}}{\partial \varepsilon_{n\mathbf{k}}}\right), \tag{2}$$

$$\boldsymbol{\kappa}_e = \frac{s}{T\Omega N_{\mathbf{k}}} \sum_{n\mathbf{k}} (\varepsilon_{n\mathbf{k}} - \varepsilon_f)^2 \mathbf{v}_{n\mathbf{k}} \mathbf{F}_{n\mathbf{k}} \left(-\frac{\partial f^0_{n\mathbf{k}}}{\partial \varepsilon_{n\mathbf{k}}}\right) - T\boldsymbol{\sigma}\boldsymbol{\alpha}^2, \tag{3}$$

where $N_{\mathbf{k}}$ is the total number of $\mathbf{k}$ points, Ω is the volume of unit cell, e is the electron charge, $f^0_{n\mathbf{k}}$ is the Fermi-Dirac distribution for $n\mathbf{k}$ state, $v_{n\mathbf{k}}$ is the electron velocity, $\varepsilon_{n\mathbf{k}}$ is the electron energy and ε_f is the chemical potential, s is the number of electrons per state. $\mathbf{F}_{n\mathbf{k}}$ is obtained from iterative solution of electron BTE,

$$\mathbf{F}^{i+1}_{n\mathbf{k}} = \tau_{n\mathbf{k}} \mathbf{v}_{n\mathbf{k}} + \frac{\tau_{n\mathbf{k}}}{N_{\mathbf{q}}} \sum_{m\mathbf{q}\nu} W^{\mathbf{q}\nu}_{n\mathbf{k},m\mathbf{k}+\mathbf{q}} \mathbf{F}^{i}_{m\mathbf{k}+\mathbf{q}}, \tag{4}$$

staring from $\mathbf{F}_{n\mathbf{k}} = \mathbf{v}_{n\mathbf{k}} \cdot \tau_{n\mathbf{k}}$ with $\tau_{n\mathbf{k}}$ being the relaxation time. $N_{\mathbf{q}}$ is the total number of $\mathbf{q}$ points, $W^{\mathbf{q}\nu}_{n\mathbf{k},m\mathbf{k}+\mathbf{q}}$ is the phonon-limited transition probability via absorption and emission processes [30]. Analogously, the $\boldsymbol{\kappa}_l$ also can be obtained from the BTE for phonon, written by

$$\boldsymbol{\kappa}_p = \frac{1}{\Omega N_{\mathbf{q}}} \sum_{\mathbf{q}p} \hbar\omega_{\mathbf{q}p} \mathbf{v}_{\mathbf{q}p} \mathbf{F}_{\mathbf{q}p} \left(\frac{\partial n^0_{\mathbf{q}p}}{\partial T}\right), \tag{5}$$

where $n^0_{\mathbf{q}p}$ is the Bose-Einstein distribution of $\mathbf{q}p$ mode, $\omega_{\mathbf{q}p}$ is the phonon frequency, $\mathbf{v}_{\mathbf{q}p}$ is the phonon velocity, $\mathbf{F}_{\mathbf{q}p}$ is the mean free displacement obtained from iterative solution of phonon BTE [2,31].

The DFT and DFPT calculations were implemented using Quantum ESPRESSO [32], and the norm-conserving pseudopotentials with Perdew-Burke-Ernzerhof (PBE) exchange-correlation functional were adopted. Although previous calculation reported that the experimental crystal structure gives a phonon dispersion more consistent with experimental measurements than that of relaxed structure with PBE [33], we still follow the standard first-principles calculations processes to fully relax the crystal structure. Since the spin orbital coupling has been proven negligible [33], it is not included in the calculations. For $\{\alpha, \sigma, \kappa_e\}$, the calculations were initially conducted on 6×10×10 $\mathbf{k}$ and 3×5×5 $\mathbf{q}$ grids to obtain the hamiltonian matrix, dynamic matrix and electron-phonon coupling matrix. The Wannier function interpolation in EPW package [8] was used to acquire the quantities on dense grids of 24×48×48 for $\mathbf{k}$ and $\mathbf{q}$ points in solving electron BTE. For κ_l, the second-order interatomic force constants (IFCs) obtained on 3×5×5 $\mathbf{q}$ grids in above DFPT calculations was used, while the third-order IFCs was calculated using 2×4×4 supercells with a cutoff distance of 0.70 nm, which is long enough to eliminate the inaccuracy of force truncation [34]. The ShengBTE [2] was used for iterative solution of phonon BTE with 24×24×24 $\mathbf{q}$ points. These above parameter settings are enough for the convergence of quantities above room temperature.

3. Results and discussions

In the weak doping limit where the defects-caused scattering is negligible as compared to the other types of relevant scattering, the calculations do not need to involve modeling of defects. However, in the doping range technologically relevant to thermoelectric materials, defects scattering affects the carriers (both electrons and phonons) lifetimes. From the Wiedemann-Franz law, the Lorenz number is defined by $L = \kappa_e/(\sigma T)$, then the ZT can be rewritten as

$$ZT = \frac{\alpha^2 n_c e T}{L n_c e T + \kappa_{\mathrm{p}}/\mu}, \tag{6}$$

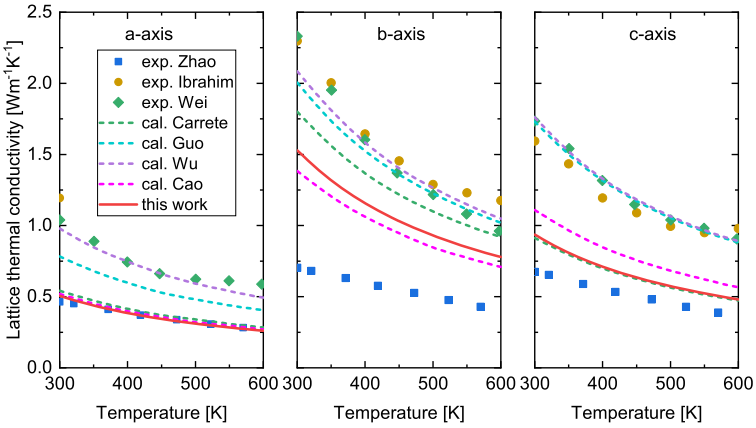

Fig. 1. Lattice thermal conductivity of SnSe along its three crystallographic axes as compared with the experimental data from Zhao et al. [18], Ibrahim et al. [39], and Wei et al. [40], and the first-principles calculations by Carrete et al. [34], Guo et al. [41], Wu et al. [42], and Cao et al. [27], respectively. (For interpretation of the colors in the figure(s), the reader is referred to the web version of this article.)

where n_c is the electron concentration, $\mu = \sigma/(n_c e)$ is the electron mobility. Among the thermoelectric quantities, α is dominated by the band structure, and thus carriers lifetimes have little effect. That is the reason that α can be accurately obtained without referring to charge carriers lifetimes [20]. In single crystal, μ is generally more sensitive to the defects than κ_l in most cases. For instance, in the high and moderate κ_l materials of BAs [35] and Si [36,37], the room-temperature μ at carrier concentration of 10^{19} cm^{-3} is more than one order of magnitude smaller than the intrinsic values while the κ_l only reduces about 50% and 20%, respectively. In low κ_l materials like Mg_2Si [38], when the doping increases the electron concentration from 10^{16} to 10^{18} cm^{-3}, the room-temperature μ decreases about one order of magnitude but the κ_l does not change significantly. On the other hand, the κ_l of the thermoelectric material itself is low, so the change in κ_l after doping will not be large, such as SnSe [18,21,23,25]. This suggests that the calculated κ_l/μ is more likely to be underestimated when the defect scattering is neglected.

According to the non-degenerate parabolic band model, $L = (k_B/e)^2(5/2 + r)$ where r is the exponent of energy dependence of scattering rate as $\tau^{-1} \propto E^{-r}$ [6,10]. For phonon-limited scattering, r is negative semidefinite. Although the scattering mechanisms caused by defects are too complicated to be accurately analyzed, two typical scatterings are clearly known to exist, *i.e.,* ionized impurity scattering and neutral defect scattering. For ionized impurity scattering, r is positive [6,17], thus ionized impurity would increase L. Recent first-principles calculations show that neutral defect results in negative r [16]. Considering the neutral defect scattering is generally weak as compared to the ionized impurity and phonon scattering [16,17], L would be little changed or underestimated when neglecting these two kinds of defects scattering. Therefore, despite the other effects of defects cannot be known, the calculated ZT from the intrinsic phonon-limited quantities may not deviate greatly from the practical ZT values. After qualitative analysis, we illustrate this point in the case of SnSe.

The low thermal conductivity is a key ingredient for the high ZT of SnSe. Experimentally measured thermal conductivity contains κ_l and κ_e. In low charge-carrier concentration limit, the contribution of κ_e is negligible and thus the measured thermal conductivity can be regarded as κ_l. Then we can collect three sets of experimental κ_l for SnSe along its *a*, *b* and *c* crystallographic axes from the literatures [18,39,40], as given in Fig. 1. The first reported thermal conductivities of SnSe in Ref. [18] are questioned not belonging to single crystal due to the low mass density of the samples therein, only about 88% of the theoretical density [43], which is later revealed stemming from the Sn vacancy [20,22]. Moreover, the measured thermal conductivity is smaller than its polycrystal systems [44,45]. However, the unusual high thermal conductivity of polycrystal is recently demonstrated to suffer from the tin oxides (SnO_x) covering the surface of SnSe, and the thermal conductivity can be reduced significantly in purified polycrystalline samples [46]. The other measurements on SnSe single crystals in Refs. [39] and [40] reported much higher thermal conductivities than those of Ref. [18].

The κ_l obtained by first-principles calculations in previous studies are also plotted for comparison [34,41,42]. These calculations are all implemented in VASP with projector augmented wave (PAW) pseudopotentials. Guo et al. [41] used 2×3×3 supercell with local density approximation (LDA) pseudopotentials, while Wu et al. [42] used 2×4×4 supercell with PBE pseudopotentials and the van der Waals (vdW) interaction was additionally included. Comparing to the results of Guo et al., Wu et al. presented similar κ_l along the *b* and *c* axes but obviously higher κ_l along the *a* axis. Carrete et al. [34] adopted 3×5×5 supercell with PBE pseudopotentials while Cao et al. [27] used 2×3×3 supercell. The obtained κ_l are obvious lower than those of Guo et al. and Wu et al. in all three directions. The discrepancy of calculations probably comes from the different structural and computational parameters. Herein, the κ_l are more consistent with those of Carrete et al. [34] and Cao et al. [27], all of them are implemented with PBE and without vdW correction. The calculated κ_l are 0.5, 1.5 and 0.9 Wm^{-1}K^{-1} at room temperature along the *a*, *b* and *c* axes, respectively.

Fig. 2 shows the calculated ZT of *n*-type SnSe at different temperatures. The ZT at carrier concentrations of 10^{17}, 10^{18}, 10^{19}, and 10^{20} cm^{-3} as well as the maximum values obtained in calculations are plotted. The maximum ZT corresponds to a carrier concentration around 10^{19} cm^{-3} for all three axes. As temperature increases from 300 to 600 K, the calculated maximum ZT of *n*-type SnSe along *a*, *b* and *c* axes increase monotonously from 0.48, 0.38, and 0.43 to 1.90, 0.91, and 1.21, respectively. The *n*-type SnSe was firstly synthesized by Duong et al. [22] with bismuth substituting Sn sites, yielding a carrier concentration of 2.1×10^{19} cm^{-3}, and the measurements give nearly identical high ZT along *b* and *c* axes, while the *a*-axis ZT is relatively small. The experimental ZT is much smaller than the predicted maximum value at room temperature, but close to that with increasing temperatures along *b* and *c* axes. In contrast to the findings of Duong et al. [22], the first-principles calculations suggest that the *a* axis should have higher ZT than *b* and *c* axes. Chang et al. [19] successfully synthesized *n*-type SnSe through the bromine doping at a concentration of 1.2×10^{19} cm^{-3}. They found much higher ZT along *a* axis, with a value of about 0.25 at room temperature. Subsequently, Su et al. [24] enhanced the *a*-axis ZT of bromine-doped SnSe by additionally introducing lead alloying, and reported a record high ZT along *a* axis using chlorine dopant instead of bromine. It can be seen that the highest values of measured ZT for *n*-type SnSe are near the maximum ZT predicted by the first-principles calculations.

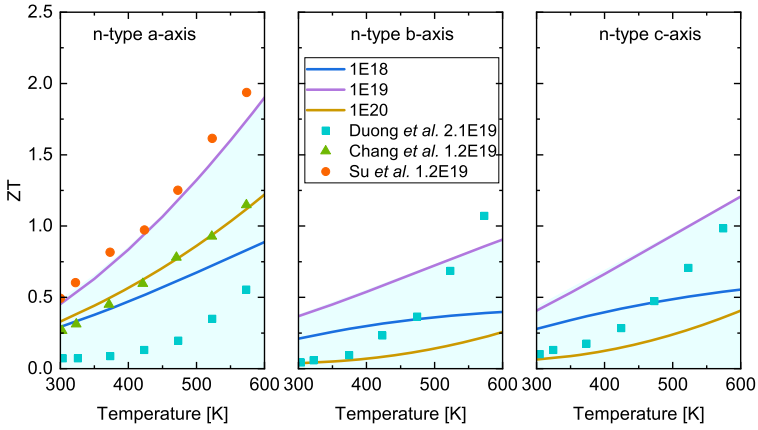

Fig. 2. Calculated ZT of *n*-type SnSe at different carrier concentrations and temperatures as compared with experimental data from Duong et al. [22], Chang et al. [19], and Su et al. [24]. The upper bound of light blue background indicates the maximum ZT obtained in calculations.

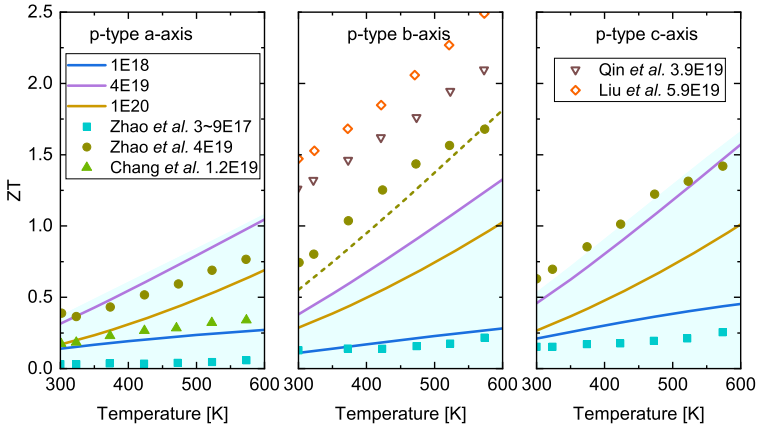

Fig. 3. Calculated ZT of *p*-type SnSe at different carrier concentrations and temperatures as compared with experimental data from Zhao et al. [18,21], Chang et al. [19], Qin et al. [23], and Liu et al. [25]. The upper limit of light blue background indicates the maximum ZT obtained in calculations. The dashed line gives the *b*-axis ZT calculated with k_l of *c* axis. Note that the open symbols indicate that the band structure of experimental samples has significantly changed, which is beyond the scope of this article.

The calculated ZT of *p*-type SnSe are compared with experimental values in Fig. 3. The maximum ZT along *a*, *b* and *c* axes from calculations are 0.37, 0.39, and 0.53 at 300 K, which increase to 1.08, 1.33, and 1.67 at 600 K, respectively. The pristine SnSe reported by Zhao et al. [18] exhibits hole concentrations of only about 3~9×10^{17} cm^{-3} in the temperature range of 300-600 K. Thus, although high ZT is found in $Cmcm$ phase, the ZT for $Pnma$ SnSe is smaller than 0.25 in all three axes. Soon afterwards, Zhao et al. [21] achieved heavy hole doping of 4×10^{19} cm^{-3} in SnSe single crystals through sodium doping, and the ZT of *p*-type SnSe are significantly increased. The ZT measured along *a* and *c* axes are close to the maximum values of calculations, whereas the measured ZT along *b* axis is much higher than the calculated upper bound. It is noticed that the measured κ_l of SnSe along the *b* axis are almost identical to that of the *c* axis [18,21], which is contrary to the calculated results with strong anisotropy. If the *c*-axis κ_l are used in the calculations of *b*-axis ZT, the obtained values can be significantly increased and close to the experimental values, as shown by the dashed line in Fig. 3. Recently, the ZT of *p*-type SnSe along *b* axis has been further improved by lead alloying [23] and copper occupying [25]. Different from the sodium doping which only generates a high hole concentration but remains the crystal lattice structure or the band structure unchanged [25,47], the lead alloying and copper occupying can effectively modulate the crystal structure and promote multi-band synglisis which further optimize the electrical transport properties [23,25]. Science the absence of such strong band engineering effect in the calculations, it is understandable that the experimental values are much higher than the calculated maximum.

The contour maps of ZT depending on temperature and carrier concentration for SnSe are given in Fig. 4. It shows that the *n*-type SnSe observes higher ZT along *a* axis than that of *b* and *c* axes, and the *a*-axis ZT goes beyond unity in a large carrier concentration and temperature range. For *p*-type SnSe, the higher ZT appears in the *b* and *c* directions, and the highest ZT that can be achieved is smaller than *n*-type SnSe due to much higher κ_l along *b* and *c* axes. In addition, the electron concentrations corresponding to the maximum ZT are about 6×10^{18}~1×10^{19} cm^{-3}, while the optimal hole concentrations are about 2~4×10^{19} cm^{-3} in the temperature range of 300-600 K. These concentrations are close to the measured concentrations of experimental SnSe samples. This implies that the calculations help to identify the optimal doping concentration to some extent.

After direct comparison between the phonon-limited ZT and experimental values, we examine the doping influence on the calculated ZT using semiempirical models. The *n*- and *p*-type SnSe are assumed by substituting Bi and Na at Sn sites, respectively [21,22]. The dopant interaction in electrical transport is considered as ionized impurity scattering using Brooks and Herring model [48], while its scattering to phonons is determined by mass disorder using the scheme as isotope scattering [12] (cf. S1 in the supplementary material). Fig. 5 presents the calculated μ, κ_l, and ZT at 500 K under different doping concentrations with and without impurity scattering. At a dopant concentration of 10^{19} cm^{-3}, the μ in *n*- and *p*-type SnSe is decreased by 10-16%,

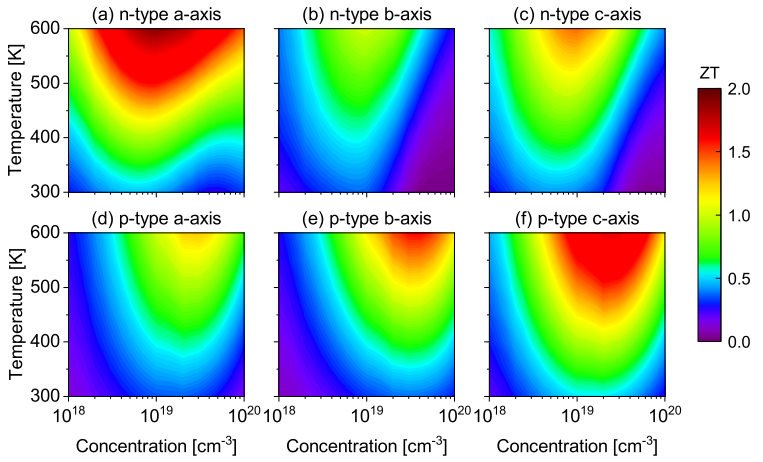

Fig. 4. Contour map of ZT as a function of temperature and carrier concentration for *n*- and *p*-type SnSe along *a*, *b* and *c* axes.

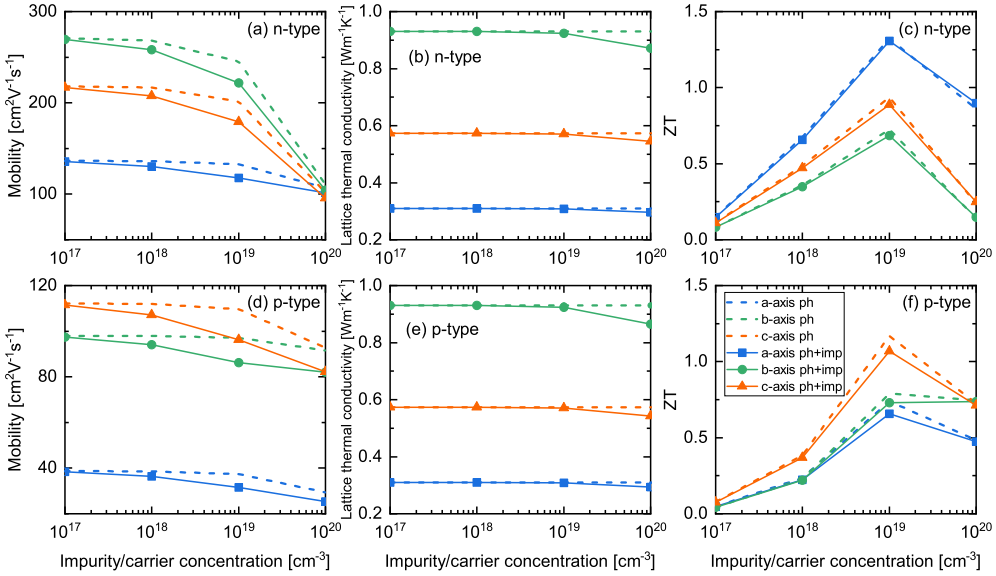

Fig. 5. Calculated (a, d) mobility, (b, e) lattice thermal conductivity, and (c, f) ZT for *n*- and *p*-type SnSe at 500 K under different doping concentrations with and without impurity scattering.

while the decrease of κ_l is within 1%. The reduction by 10^{20} cm^{-3} doping is 5-14% for μ and 5-7% for κ_l. This is in line with the general experience stated above that μ is more sensitive to defects than κ_l. Correspondingly, the decrease of ZT is smaller than 10% and 6% in all three directions under 10^{19} and 10^{20} cm^{-3} doping concentrations, respectively. Although the doping scattering is only approximately estimated, the results still indicate to a certain extent that the change of calculated ZT by doping defects is somewhat weakened compared to the electrical transport properties. Therefore, the speculation about ZT in Eq. (6) can be confirmed to a considerable extent.

Adjusting the pressures on the crystals has been long recognized as an important scheme to modulate their lattice structure and thus electrical and thermal transport properties. By applying pressures on moderately hole-doped SnSe with carrier concentration of about 2×10^{18} cm^{-3}, Nishimura et al. [28] experimentally found that the in-plane (*b*-*c* plane) thermoelectric power factor, $PF = \alpha^2\sigma T$, obtained a large enhancement over a wide temperature range from 10 to 300 K. The room-temperature PF increases from 5 μWcm^{-1}K^{-2} at ambient pressure to 12 μWcm^{-1}K^{-2} at 1.6 GPa pressure. Here, we calculated the thermoelectric properties of *n*- and *p*-type SnSe at pressures of 1.6 GPa and 3.2 GPa. As expected, the lattice constants decrease with increasing pressures, from basic parameters of $a = 11.72$ Å, $b = 4.21$ Å, $c = 4.49$ Å to $a = 11.51$ Å, $b = 4.18$ Å, $c = 4.37$ Å under 1.6 GPa pressure and $a = 11.37$ Å, $b = 4.16$ Å, $c = 4.28$ Å under 3.2 GPa pressure.

Fig. 6 shows the pressure dependent PF of *n*- and *p*-type SnSe as a function of carrier concentrations at room temperature. For *p*-type SnSe, with increase of pressure, the PF along the *b* axis increases significantly, followed by the *c* axis and *a* axis but much less than the increase in the *b* axis. At hole concentration of 2×10^{18} cm^{-3}, the calculated room-temperature PF along *b* axis is 8.5 μWcm^{-1}K^{-2} with no pressure applied and 13.4 μWcm^{-1}K^{-2} under 1.6 GPa, which are roughly consistent with the experiment findings [28]. The maximum PF of *p*-type SnSe along *b* axis is enhanced from 30 to 47 and 90 μWcm^{-1}K^{-2} by 1.6 and 3.2 GPa pressures, respectively. In contrast, for *n*-type SnSe, the pressure-induced PF enhancement is mainly manifested in the *a*-axis direction, but there is no significant improvement in the *b* and *c* axes. At an electron concentration of 10^{19} cm^{-3}, the room-temperature PF can be increased from 12 to 34 μWcm^{-1}K^{-2} by 1.6 GPa pressure and to 59 μWcm^{-1}K^{-2} by 3.2 GPa pressure. The anisotropic enhancement of PF can be understood from the nonmonotonic influence of pressure on σ and α. For *p*-type SnSe, as pressure increases, the σ in all three axes increase, but the α in *a* and *c* axes decrease obviously (Fig. S1 and S2 in

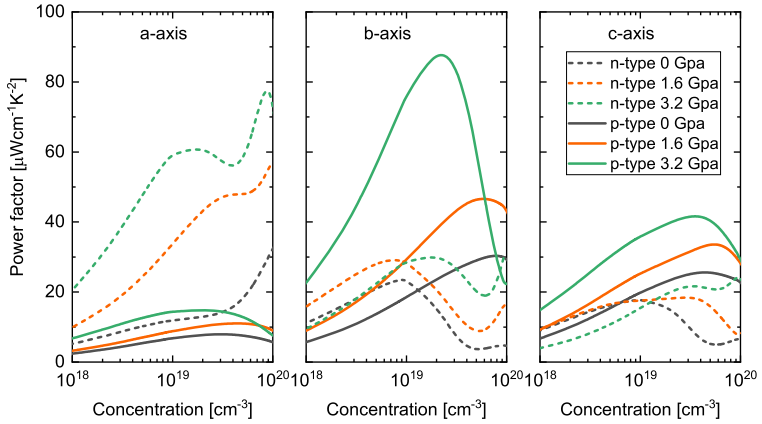

Fig. 6. Calculated room-temperature PF of n- and p-type SnSe at different carrier concentrations and pressures.

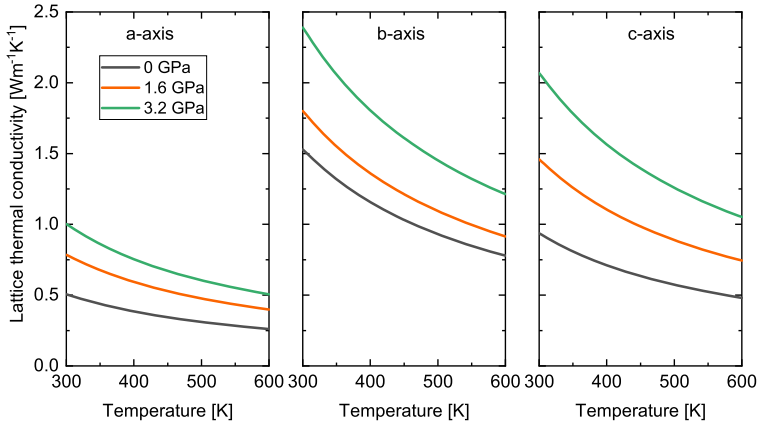

Fig. 7. Calculated κ_p of SnSe at different temperatures and pressures.

the supplementary material). As a result, only the b-axis PF has significant enhancement while the increase in other axes is weak. The change of σ and α in n-type SnSe is different from that of p-type SnSe. When a pressure of 3.2 GPa is applied, the α increases in all axes, while the σ only increases in a axis but reduces in b and c axes (Fig. S1 and S2 in the supplementary material). Then, the PF of n-type SnSe along a-axis direction gains a large enhancement but the other axes do not. In addition, following the change trend of σ under increasing pressure, the μ at low concentration of p-type SnSe is increased in all three axes. In n-type SnSe, the μ increases in a axis but decreases in c axes, while the b-axis μ is increased by 1.6 GPa but decreased by 3.2 GPa pressure (Fig. S4 in the supplementary material).

In addition to the electrical transport properties, the pressure also alters the phonon transport of SnSe. Fig. 7 presents the calculated κ_l of SnSe at different pressures. It can be seen that the κ_l increases monotonically in all three axes as pressure increases up to 3.2 GPa, in consistent with the results of Ref. [27] for SnSe and its analogue of SnS [49]. At 1.6 GPa pressure, the room-temperature κ_l are 0.8, 1.8 and 1.5 $Wm^{-1}K^{-1}$ along a, b and c axes, respectively, while the values are 1.1, 2.4 and 2.1 $Wm^{-1}K^{-1}$ under 3.2 GPa pressure. The relation of $\kappa_l^b > \kappa_l^c > \kappa_l^a$ remains when the pressures applied. But the anisotropy of κ_l^b/κ_l^c decreases from 1.7 with no pressure applied to 1.2 and 1.1 under 1.6 and 3.2 GPa, respectively. Following the usual rules, the pressure compresses the lattice structure, which stiffens the phonon dispersion and thus increases the phonon velocity. This can be seen from the averaged phonon velocities of SnSe under different pressures (Fig. S5 in the supplementary material). The increased pressure also decreases the anharmonicity of phonons below 5 rad·ps^{-1} and slightly increases the anharmonicity above this frequency, as revealed by the Grüneisen parameters (Fig. S6(a) in the supplementary material). The scattering phase space for phonons below 5 rad·ps^{-1} is suppressed by pressures, and it is increased for phonons between 5 and 12 rad·ps^{-1}, after which it again decreases for phonons with frequency up to 20 rad·ps^{-1} (Fig. S6(b) in the supplementary material). Thus, the scattering rates, proportional to the anharmonicity and scattering phase space, of phonons below 20 rad·ps^{-1} are overall decreased slightly by pressures (Fig. S6(c) in the supplementary material). Meanwhile, these phonons with frequency smaller than 20 rad·ps^{-1} contribute most of the κ_l, more than 62%, 70% and 73% under pressures of 0 GPa, 1.6 GPa and 3.2 GPa, respectively (Fig. S7 in the supplemental material). As a result, the increased phonon velocity and the reduced phonon scattering rate raise the κ_l of SnSe. Therefore, although the pressure enormously improves the PF of n- and p-type SnSe along a and b axes, respectively, the increased κ_l gives rise to a negative influence on the ZT value.

Fig. 8 shows the influences of pressures on the ZT of n- and p-type SnSe at room temperature. For n-type SnSe, the pressure induced enhancement of PF in the b and c axes is small. Although the b- and c-axis κ_e are decreased by pressure, at 10^{19} cm^{-3} concentration, the κ_e is smaller than 0.5 $Wm^{-1}K^{-1}$ (Fig. S3 in the supplementary material), which means that the total thermal conductivity is dominated by κ_l. Therefore, the small enhancement of PF is not enough to offset the deterioration from the increased κ_l, so the ZT value decreases slightly with the increase of pressure. Nevertheless, in the a-axis direction, the huge enhancement in PF still guarantees an increase in the ZT value. The maximum ZT of n-type SnSe along a axis is improved to 0.87 at an electron concentration around 10^{19} cm^{-3} by 1.6 GPa pressure, while the value at 3.2 GPa pressure is 1.2 around the concentration of 8×10^{18} cm^{-3}. The effect of pressure on p-type SnSe shows similar changes due

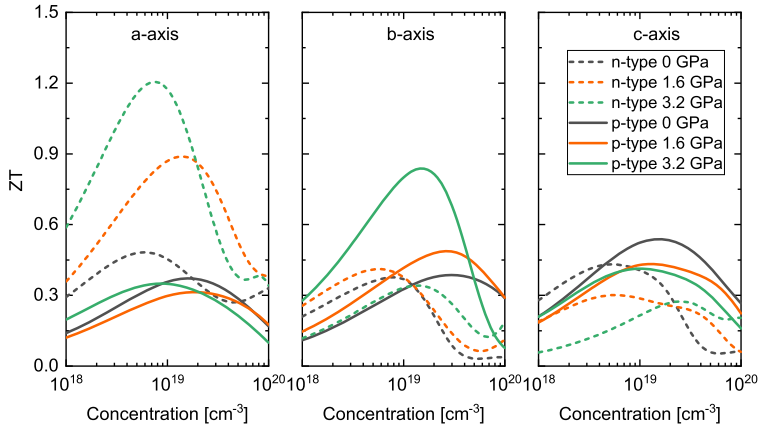

Fig. 8. Calculated room-temperature ZT of *n*- and *p*-type SnSe at different carrier concentrations and pressures.

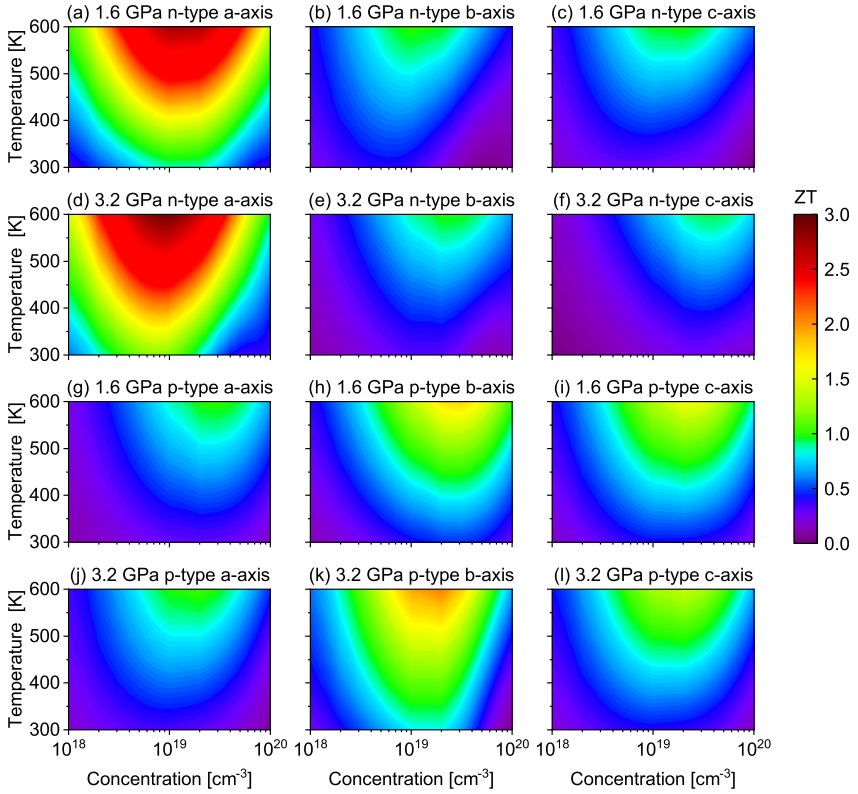

Fig. 9. Contour map of ZT as a function of temperature and carrier concentration for SnSe under 1.6 and 3.2 GPa pressures. (a-f) are for *n*-type SnSe and (g-l) are for *p*-type SnSe along *a*, *b* and *c* axes.

to increased κ_e and κ_l, but mainly has significant improvement in the *b*-axis ZT. The maximum ZT of *p*-type SnSe along *b* axis are 0.49 and 0.82 under pressures of 1.6 and 3.2 GPa, respectively. The corresponding hole concentrations are 3×10^{19} and 2×10^{19} cm^{-3}, respectively. The anisotropy of ZT under pressures becomes stronger as compared to that of original SnSe [27]. Applying 1.6 and 3.2 GPa pressures on *n*-type SnSe can enhance the ZT along *a* axis by 81% and 150%, respectively. Likewise, the increases of ZT for *p*-type SnSe along *b* axis are 26% and 110%, respectively.

The temperature and carrier concentration dependence of ZT for *n*- and *p*-type SnSe under pressures of 1.6 and 3.2 GPa are depicted in Fig. 9. It can be seen that the enhancement of ZT by increased pressure persists from low to high temperatures, mainly on the *a* axis of *n*-type SnSe and *b* axis of *p*-type SnSe. At 600 K, the *a*-axis ZT for *n*-type SnSe are 2.7 and 2.9 under pressures of 1.6 and 3.2 GPa, respectively, while the ZT are 1.6 and 1.8 for *p*-type SnSe along *b* axis. By applying pressure up to 3.2 GPa, the ZT at 600 K are increased by 53% and 38% for *n*-type SnSe along *a* axis and *p*-type SnSe along *b* axis, respectively. For *p*-type SnSe, the pressure induces the ZT along *b* axis to become larger than that of *c* axis, due to the reduced anisotropy of κ_l of *b* and *c* axes. In addition, the optimal carrier concentration corresponding to the highest ZT does not change significantly with the change of temperature and pressure. The calculated optimal concentrations under 1.6 and 3.2 GPa for *n*-type *a*-axis ZT are from 6×10^{18} to 1×10^{19} cm^{-3} in the temperature range of 300-600 K, while the optimal concentrations are from 2×10^{19} to 4×10^{19} cm^{-3} for *p*-type *b*-axis ZT. These calculated concentrations are close to the doping concentrations that have been experimentally achieved so for, indicating that it is feasible to further induce the enhancement of ZT for SnSe by pressure.

4. Conclusions

The intrinsic electrical and thermal transport properties of *Pnma* SnSe were obtained from the iterative Boltzmann transport equations combined with first-principles calculated electron-phonon and phonon-phonon limited scatterings. The qualitative analysis argues that the ZT without including the defect scattering may not deviate greatly from the practical values. The phonon-limited ZT of *n*- and *p*-type SnSe were calculated, which indeed a certain degree of quantitatively reproduced the experimental values. The reasonable agreement between intrinsic calculations and practical measurements verifies that the phonon-limited ZT can serve as a good assessment of actual thermoelectric performance of single crystals. This provides an effective way to predict the ZT promise of thermoelectric materials, and also suggests optimal carrier concentration ranges for experimental synthesization. Then, the influence of pressure on the thermoelectric performance of SnSe was investigated. The lattice thermal conductivity of SnSe increases monotonically as pressure increases due to increased phonon velocity and decreased phonon scattering. The thermoelectric power factor of SnSe is also increased by pressure, and is significant in the *a* axis of *n*-type SnSe and *b* axis of *p*-type SnSe, but weak along other axial directions. The huge enhancement in thermoelectric power factor offsets the deterioration from the increased lattice thermal conductivity, yielding an increase in the ZT. At room temperature, the *a*-axis ZT of *n*-type SnSe is increased from 0.48 to 0.87 and 1.20, while the *b*-axis ZT of *p*-type SnSe is increased from 0.39 to 0.49 and 0.82, by applying pressures of 1.6 and 3.2 GPa, respectively. The pressure induced enhancement of ZT hold at high temperatures. The corresponding electron and hole carrier concentrations for the optimal thermoelectric performance are around 10^{19} cm^{-3} in the temperature range of 300-600 K and do not change significantly by pressures.

CRediT authorship contribution statement

Jinlong Ma: Conceptualization, Investigation, Software, Writing – original draft. **Yani Chen:** Writing – review & editing. **Wu Li:** Conceptualization, Validation, Writing – review & editing. **Xiaobing Luo:** Resources, Supervision.

Declaration of competing interest

The authors declare that they have no known competing financial interests or personal relationships that could have appeared to influence the work reported in this paper.

Data availability

Data will be made available on request.

Acknowledgement

J.M. acknowledges support from the Hubei Provincial Natural Science Foundation of China (Grant No. 2022CFB104). Y.C. and W.L. acknowledge support from the National Natural Science Foundation of China (Grants No. 12174261 and No. 12104312), and Natural Science Foundation of Guangdong Province (Grants No. 2023A1515010365 and No. 2022A1515011877).

Appendix A. Supplementary material

Supplementary material related to this article can be found online at https://doi.org/10.1016/j.ijheatmasstransfer.2023.125063.

References

[1] D.A. Broido, M. Malorny, G. Birner, N. Mingo, D.A. Stewart, Intrinsic lattice thermal conductivity of semiconductors from first principles, Appl. Phys. Lett. 91 (23) (2007) 231922.
[2] W. Li, J. Carrete, N.A. Katcho, N. Mingo, Shengbte: a solver of the Boltzmann transport equation for phonons, Comput. Phys. Commun. 185 (6) (2014) 1747–1758.
[3] Z. Han, X. Yang, W. Li, T. Feng, X. Ruan, Fourphonon: an extension module to shengbte for computing four-phonon scattering rates and thermal conductivity, Comput. Phys. Commun. 270 (2022) 108179.
[4] A. van Roekeghem, J. Carrete, C. Oses, S. Curtarolo, N. Mingo, High-throughput computation of thermal conductivity of high-temperature solid phases: the case of oxide and fluoride perovskites, Phys. Rev. X 6 (2016) 041061.
[5] A. She, Y. Zhao, J. Ni, S. Meng, Z. Dai, Investigation on transport properties and anomalously heat-carrying optical phonons in kxy (x = ca, mg; y = sb, bi), Int. J. Heat Mass Transf. 209 (2023) 124132.
[6] B. Qiu, Z. Tian, A. Vallabhaneni, B. Liao, J.M. Mendoza, O.D. Restrepo, X. Ruan, G. Chen, First-principles simulation of electron mean-free-path spectra and thermoelectric properties in silicon, Europhys. Lett. 109 (5) (2015) 57006.
[7] J. Ma, A.S. Nissimagoudar, W. Li, First-principles study of electron and hole mobilities of si and gaas, Phys. Rev. B 97 (2018) 045201.
[8] S. Poncé, E. Margine, C. Verdi, F. Giustino, Epw: electron-phonon coupling, transport and superconducting properties using maximally localized Wannier functions, Comput. Phys. Commun. 209 (2016) 116–133.
[9] S. Poncé, W. Li, S. Reichardt, F. Giustino, First-principles calculations of charge carrier mobility and conductivity in bulk semiconductors and two-dimensional materials, Rep. Prog. Phys. 83 (3) (2020) 036501.
[10] J. Park, Y. Xia, V. Ozoliņš, High thermoelectric power factor and efficiency from a highly dispersive band in Ba_2BiAu, Phys. Rev. Appl. 11 (1) (2019) 014058.
[11] J. Ma, A.S. Nissimagoudar, S. Wang, W. Li, High thermoelectric figure of merit of full-Heusler ba2aux (x = as, sb, and bi), Phys. Status Solidi RRL 14 (6) (2020) 2000084.
[12] S. Li, Z. Tong, H. Bao, Resolving different scattering effects on the thermal and electrical transport in doped snse, J. Appl. Phys. 126 (2) (2019) 025111.
[13] S. Zeng, Q. Shen, L. Fang, Z. Gu, J. Yang, G. Li, Y. Tu, J. Ni, Room temperature high thermoelectric performance of bi-based full-Heusler compounds csxrb3-xbi with strong anharmonicity, Int. J. Heat Mass Transf. 217 (2023) 124628.
[14] A. Katre, J. Carrete, B. Dongre, G.K.H. Madsen, N. Mingo, Exceptionally strong phonon scattering by b substitution in cubic sic, Phys. Rev. Lett. 119 (2017) 075902.
[15] A. Katre, J. Carrete, T. Wang, G.K.H. Madsen, N. Mingo, Phonon transport unveils the prevalent point defects in gan, Phys. Rev. Mater. 2 (2018) 050602.
[16] I.-T. Lu, J.-J. Zhou, M. Bernardi, Efficient ab initio calculations of electron-defect scattering and defect-limited carrier mobility, Phys. Rev. Mater. 3 (2019) 033804.
[17] I.-T. Lu, J.-J. Zhou, J. Park, M. Bernardi, First-principles ionized-impurity scattering and charge transport in doped materials, Phys. Rev. Mater. 6 (2022) L010801.
[18] L.-D. Zhao, S.-H. Lo, Y. Zhang, H. Sun, G. Tan, C. Uher, C. Wolverton, V.P. Dravid, M.G. Kanatzidis, Ultralow thermal conductivity and high thermoelectric figure of merit in snse crystals, Nature 508 (2014) 373–377.
[19] C. Chang, M. Wu, D. He, Y. Pei, C.-F. Wu, X. Wu, H. Yu, F. Zhu, K. Wang, Y. Chen, L. Huang, J.-F. Li, J. He, L.-D. Zhao, 3d charge and 2d phonon transports leading to high out-of-plane zt in n-type snse crystals, Science 360 (6390) (2018) 778–783.
[20] A. Dewandre, O. Hellman, S. Bhattacharya, A.H. Romero, G.K.H. Madsen, M.J. Verstraete, Two-step phase transition in snse and the origins of its high power factor from first principles, Phys. Rev. Lett. 117 (2016) 276601.
[21] L.-D. Zhao, G. Tan, S. Hao, J. He, Y. Pei, H. Chi, H. Wang, S. Gong, H. Xu, V.P. Dravid, C. Uher, G.J. Snyder, C. Wolverton, M.G. Kanatzidis, Ultrahigh power factor and thermoelectric performance in hole-doped single-crystal snse, Science 351 (6269) (2016) 141–144.
[22] A.T. Duong, V.Q. Nguyen, G. Duvjir, V.T. Duong, S. Kwon, J.Y. Song, J.K. Lee, J.E. Lee, S. Park, T. Min, J. Lee, J. Kim, S. Cho, Achieving zt = 2.2 with bi-doped n-type snse single crystals, Nat. Commun. 7 (2016) 13713.
[23] B. Qin, D. Wang, X. Liu, Y. Qin, J.-F. Dong, J. Luo, J.-W. Li, W. Liu, G. Tan, X. Tang, J.-F. Li, J. He, L.-D. Zhao, Power generation and thermoelectric cooling enabled by momentum and energy multiband alignments, Science 373 (6554) (2021) 556–561.
[24] L. Su, D. Wang, S. Wang, B. Qin, Y. Wang, Y. Qin, Y. Jin, C. Chang, L.-D. Zhao, High thermoelectric performance realized through manipulating layered phonon-electron decoupling, Science 375 (6587) (2022) 1385–1389.
[25] D. Liu, D. Wang, T. Hong, Z. Wang, Y. Wang, Y. Qin, L. Su, T. Yang, X. Gao, Z. Ge, B. Qin, L.-D. Zhao, Lattice plainification advances highly effective snse crystalline thermoelectrics, Science 380 (6647) (2023) 841–846.
[26] Y. Zhang, S. Hao, L.-D. Zhao, C. Wolverton, Z. Zeng, Pressure induced thermoelectric enhancement in snse crystals, J. Mater. Chem. A 4 (2016) 12073–12079.
[27] W. Cao, Z. Wang, L. Miao, J. Shi, R. Xiong, Extremely anisotropic thermoelectric properties of snse under pressure, Energy Environ. Mater. 6 (3) (2023) e12361.
[28] T. Nishimura, H. Sakai, H. Mori, K. Akiba, H. Usui, M. Ochi, K. Kuroki, A. Miyake, M. Tokunaga, Y. Uwatoko, K. Katayama, H. Murakawa, N. Hanasaki, Large enhancement of thermoelectric efficiency due to a pressure-induced Lifshitz transition in snse, Phys. Rev. Lett. 122 (2019) 226601.
[29] G.K. Madsen, D.J. Singh, Boltztrap. A code for calculating band-structure dependent quantities, Comput. Phys. Commun. 175 (1) (2006) 67–71.
[30] W. Li, Electrical transport limited by electron-phonon coupling from Boltzmann transport equation: an ab initio study of si, al, and mos_2, Phys. Rev. B 92 (2015) 075405.
[31] J. Ma, W. Li, X. Luo, Examining the Callaway model for lattice thermal conductivity, Phys. Rev. B 90 (2014) 035203.

[32] P. Giannozzi, O. Andreussi, T. Brumme, et al., Advanced capabilities for materials modelling with quantum espresso, J. Phys. Condens. Matter 29 (46) (2017) 465901.
[33] J. Ma, Y. Chen, W. Li, Intrinsic phonon-limited charge carrier mobilities in thermoelectric snse, Phys. Rev. B 97 (2018) 205207.
[34] J. Carrete, N. Mingo, S. Curtarolo, Low thermal conductivity and triaxial phononic anisotropy of snse, Appl. Phys. Lett. 105 (10) (2014) 101907.
[35] J. Shin, G.A. Gamage, Z. Ding, K. Chen, F. Tian, X. Qian, J. Zhou, H. Lee, J. Zhou, L. Shi, T. Nguyen, F. Han, M. Li, D. Broido, A. Schmidt, Z. Ren, G. Chen, High ambipolar mobility in cubic boron arsenide, Science 377 (6604) (2022) 437–440.
[36] C. Jacoboni, C. Canali, G. Ottaviani, A. Alberigi Quaranta, A review of some charge transport properties of silicon, Solid-State Electron. 20 (2) (1977) 77–89.
[37] B. Dongre, J. Carrete, S. Wen, J. Ma, W. Li, N. Mingo, G.K.H. Madsen, Combined treatment of phonon scattering by electrons and point defects explains the thermal conductivity reduction in highly-doped si, J. Mater. Chem. A 8 (2020) 1273–1278.
[38] J.-Y. Jung, I.-H. Kim, Synthesis and thermoelectric properties of n-type mg2si, Electro. Mater. Lett. 6 (2010) 187–191.
[39] D. Ibrahim, J.-B. Vaney, S. Sassi, C. Candolfi, V. Ohorodniichuk, P. Levinsky, C. Semprimoschnig, A. Dauscher, B. Lenoir, Reinvestigation of the thermal properties of single-crystalline snse, Appl. Phys. Lett. 110 (3) (2017) 032103.
[40] P.-C. Wei, S. Bhattacharya, Y.-F. Liu, F. Liu, J. He, Y.-H. Tung, C.-C. Yang, C.-R. Hsing, D.-L. Nguyen, C.-M. Wei, M.-Y. Chou, Y.-C. Lai, T.-L. Hung, S.-Y. Guan, C.-S. Chang, H.-J. Wu, C.-H. Lee, W.-H. Li, R.P. Hermann, Y.-Y. Chen, A.M. Rao, Thermoelectric figure-of-merit of fully dense single-crystalline snse, ACS Omega 4 (2019) 5442–5450.
[41] R. Guo, X. Wang, Y. Kuang, B. Huang, First-principles study of anisotropic thermoelectric transport properties of iv-vi semiconductor compounds snse and sns, Phys. Rev. B 92 (2015) 115202.
[42] D. Wu, L. Wu, D. He, L.-D. Zhao, W. Li, M. Wu, M. Jin, J. Xu, J. Jiang, L. Huang, Y. Zhu, M.G. Kanatzidis, J. He, Direct observation of vast off-stoichiometric defects in single crystalline snse, Nano Energy 35 (2017) 321–330.
[43] P.-C. Wei, S. Bhattacharya, J. He, S. Neeleshwar, R. Podila, Y.Y. Chen, A.M. Rao, The intrinsic thermal conductivity of snse, Nature 539 (2016) E1–E2.
[44] C.-L. Chen, H. Wang, Y.-Y. Chen, T. Day, G.J. Snyder, Thermoelectric properties of p-type polycrystalline snse doped with ag, J. Mater. Chem. A 2 (2014) 11171–11176.
[45] Y.K. Lee, K. Ahn, J. Cha, C. Zhou, H.S. Kim, G. Choi, S.I. Chae, J.-H. Park, S.-P. Cho, S.H. Park, Y.-E. Sung, W.B. Lee, T. Hyeon, I. Chung, Enhancing p-type thermoelectric performances of polycrystalline snse via tuning phase transition temperature, J. Am. Chem. Soc. 139 (31) (2017) 10887–10896.
[46] C. Zhou, Y.K. Lee, Y. Yu, S. Byun, Z.-Z. Luo, H. Lee, B. Ge, Y.-L. Lee, X. Chen, J.Y. Lee, O. Cojocaru-Mirédin, H. Chang, J. Im, S.-P. Cho, M. Wuttig, V.P. Dravid, M.G. Kanatzidis, I. Chung, Polycrystalline snse with a thermoelectric figure of merit greater than the single crystal, Nat. Mater. 20 (2021) 1378–1384.
[47] W. He, D. Wang, H. Wu, Y. Xiao, Y. Zhang, D. He, Y. Feng, Y.-J. Hao, J.-F. Dong, R. Chetty, L. Hao, D. Chen, J. Qin, Q. Yang, X. Li, J.-M. Song, Y. Zhu, W. Xu, C. Niu, X. Li, G. Wang, C. Liu, M. Ohta, S.J. Pennycook, J. He, J.-F. Li, L.-D. Zhao, High thermoelectric performance in low-cost sns0.91se0.09 crystals, Science 365 (6460) (2019) 1418–1424.
[48] J. Ma, W. Li, X. Luo, First-principles study of the drift and Hall mobilities of perovskite $basno_3$, Phys. Rev. B 106 (2022) 045201.
[49] N. Ouyang, C. Wang, Y. Chen, Temperature- and pressure-dependent phonon transport properties of sns across phase transition from machine-learning interatomic potential, Int. J. Heat Mass Transf. 192 (2022) 122859.